

Cite this: *RSC Sustainability*, 2025, 3, 5326

A single-material strategy: graphene sponge bioanode and cathode for *Shewanella oneidensis* MR-1 microbial fuel cells

Konstantin G. Nikolaev,^a Jiqiang Wu,^a Xuanye Leng,^{ab} Ricardo J. Vazquez,^{id a} Samantha R. McCuskey,^{ac} Guillermo C. Bazan,^{ac} Kostya S. Novoselov^{ab} and Daria V. Andreeva^{id *ab}

Microbial fuel cells (MFCs) enable conversion of organic matter chemical energy to electricity and provide a great opportunity to upscale green energy production. However, fabricating MFCs with high power output demands strong electrode surface modification with metal nanostructures, for both the anode and cathode. Here, we propose a rational strategy to use different functionalities of graphene sponge in *Shewanella oneidensis* MR-1 MFCs. In such a fuel cell, a graphene sponge functions as a bioanode and an oxygen reduction reaction (ORR) catalyst. The ORR activity of the graphene reaches 98 mV dec⁻¹, which is comparable to that of bare Pt electrodes. The maximum power density is 184 μW cm⁻², and the current density is 753 μA cm⁻², which is comparable with MFCs based on a Pt/C cathode (50 μW cm⁻² and 280 μA cm⁻²). Furthermore, the MFC equipped with the free-standing graphene electrodes has a coulombic efficiency of 70%.

Received 28th July 2025
Accepted 13th September 2025

DOI: 10.1039/d5su00629e

rsc.li/rscsus

Sustainability spotlight

Microbial fuel cells (MFCs) offer a pathway to decentralized, carbon-neutral energy generation, but their scalability is hindered by reliance on complex, non-recyclable electrodes incorporating precious metals. This study presents a fully carbon-based, metal-free MFC design employing a graphene sponge as both a bioanode and a cathode. These freestanding electrodes deliver competitive power density and coulombic efficiency relative to Pt-based systems, while enabling recyclability and minimizing environmental impact. By eliminating critical raw materials and simplifying end-of-life processing, this work provides a sustainable and scalable route for the advancement of bioelectrochemical energy technologies.

Introduction

The explosive growth of green energy materials has gained unprecedented momentum in recent years, driven by the escalating concerns surrounding fossil fuel depletion and climate change. To address these challenges, composite materials with complex constituents have been proposed for energy conversion systems. However, despite the high power outputs achievable in fuel cells, the disposal and recycling of composite electrodes remain challenges. Among different systems, microbial fuel cells (MFCs)^{1–6} are particularly difficult to optimize, as achieving a balance between efficiency, biocompatibility, and recyclability is complicated by the energy-intensive fabrication of their composite electrodes and their dependence on environmental

water. Thus, a central challenge in MFCs design is to identify functional materials that minimize or eliminate post-use reprocessing without sacrificing power output.

In this study, we construct an MFC using graphene sponge loaded with *S. oneidensis* MR-1 (ref. 7 and 8) as a bioanode and graphene sponge cathode as a catalyst. Graphene sponges are extensively utilised in various green energy technologies, improving the efficiency and sustainability of renewable energy technologies while reducing environmental impacts.^{9–11} Among graphene derivatives^{12,13} reduced graphene oxide (rGO)^{14,15} combines sufficient electrical conductivity and surface hydrophilicity,^{16,17} which makes it suitable for bioelectrochemical systems. The optimization of rGO surface properties for bio-related applications was accomplished by self-assembly of graphene oxide (GO) flakes into a multilayer structure, followed by swelling and freeze-drying to generate a sponge-like porous morphology. Either thermal or chemical reduction of GO can then be employed to achieve a hydrophilic/hydrophobic balance and optimal conductivity. Ref. 18 provides information about the proposed optimization process. The graphene sponge macropores enhance electrochemical reactions and serve as the

^aInstitute for Functional Intelligent Materials, National University of Singapore, Singapore 117575, Singapore. E-mail: daria@nus.edu.sg^bDepartment of Materials Science and Engineering, National University of Singapore, Singapore 117575, Singapore^cDepartment of Chemistry, Chemical & Biomolecular Engineering, National University of Singapore, Singapore 119077, Singapore

primary unit in a hierarchically porous architecture for a larger specific surface area, thus increasing the bacterial electron transfer rate. Due to its three-dimensional architecture, graphene sponge provides high-density *S. oneidensis* MR-1 and enables MFCs with improved power output and coulombic efficiency.

Experimental section

Materials and instruments

S. oneidensis MR-1 (ATCC 700550), agar medium, Nafion 117 membrane, Shewanella Basal Media (SBM), sodium (L)-lactate, sodium fumarate dibasic, sulfuric acid, ethanol, sodium hydroxide, HEPES buffer, potassium phosphate monobasic, magnesium sulfate heptahydrate, ammonium chloride, potassium phosphate dibasic, ammonium sulfate, casamino acid, vitamin mix, Wolfe's mineral mix and other reagents were purchased from Sigma Aldrich. A VersaSTAT 3 Potentiostat Galvanostat, VersaSTAT 3F Potentiostat Galvanostat (AMETEK Scientific Instruments) and VMP-300 Potentiostat (Biologic) were used for electrochemical measurements. The classical rotating-disk Koutecky–Levich analysis is not applicable for the macroporous graphene sponge cathode. The Levich model assumes a smooth planar thin film with a single hydrodynamic boundary layer; rotation of a 3D sponge does not impose a uniform diffusion layer within the internal porosity and the true active area is indeterminate ($A_{\text{int}} \gg A_{\text{geo}}$). We therefore identify two ORR “onsets” from the emergence of faradaic current (tangent method) and from peaks in dI/dE , observed at ~ 0.7 and ~ 1.2 V vs. RHE. These two inflection points are consistent with a peroxide-first sequential pathway: $\text{O}_2 \rightarrow \text{HO}_2^-$ ($2e^-$) followed by $\text{HO}_2^- \rightarrow \text{OH}^-$ (additional $2e^-$) on distinct carbon sites within the sponge. A LEICA DMI6000 CS microscope (Leica) and scanning electron microscope Zeiss Sigma (Zeiss) were used for surface characterisation.

Conductive graphene sponge synthesis and *S. oneidensis* MR-1 culturing

The conductive graphene sponge preparation, as well as bacteria inoculation, is described in our previous work.¹⁸ The 0.2 wt% aqueous GO dispersion is frozen thoroughly using liquid nitrogen and immediately transferred into a freeze drier for 72 h lyophilisation to obtain the graphene-based sponge. The graphene-based bioanode scaffold is finally fabricated by thermally reducing the graphene-based sponge in a furnace tube under an Ar/H₂ inert atmosphere at 375 °C for 3 h. The specific surface area of the graphene sponge is found to be 139.2 m² g⁻¹ (Fig. 1 and S1).

S. oneidensis MR-1 (ATCC 700550) bacterial glycerol stock is stored at -80 °C. Frozen *S. oneidensis* MR-1 was placed into Luria–Bertani (LB) broth and then incubated for 24 h at 30 °C with shaking. Isolated single colonies of the bacteria on the agar plate are inoculated into the Shewanella Basal Media (SBM) containing 20 mM sodium fumarate and 20 mM sodium (L)-lactate, where oxygen in the SBM is removed by inert gas (Ar or N₂) purging for 15 min before inoculation. After 24 h of growth,

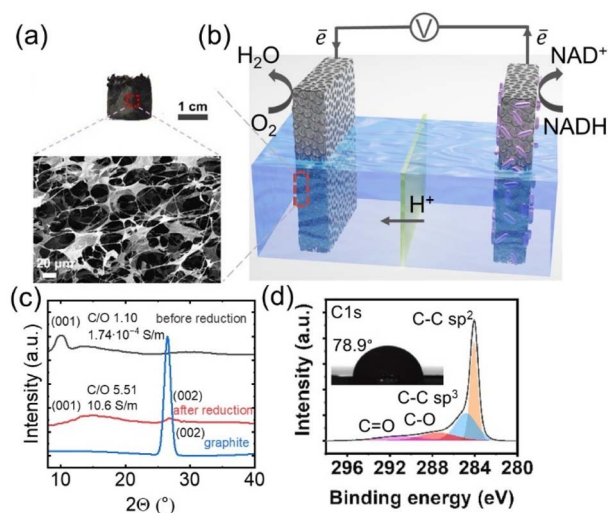


Fig. 1 (a) Optical image of the graphene electrode (upper) and SEM image of its porous sponge morphology. (b) Scheme of the MFC consists of graphene sponge cathode and bioanode. (c) Characterization of the graphene sponge before reduction, and after reduction at 375 °C with C atom to O atom ratio and conductivity. (d) XPS spectra and contact angle data (inset). Yellow, blue, red, and pink refer to sp² carbon, sp³ carbon, C–O, and C=O groups, respectively. (a, c and d) Reprinted with permission from ref. 18.

the bacterial culture was resuspended with fresh SBM medium containing 20 mM sodium (L)-lactate to a concentration of 1 OD₆₀₀ (optical density at 600 nm, $ca. 3 \times 10^8$ cells mL⁻¹) for usage. The biomass quantification was characterized by the Coomassie Protein Reagent method. Electrodes were soaked in 2 mL of 0.2 M NaOH (aq) at 4 °C for 1 h, with brief vortexing (10 s) every 15 min. The NaOH was then replaced with 2 mL SBM containing 20 mM lactate to rinse the electrodes. For cell lysis, the electrodes in SBM underwent three freeze–thaw cycles (-80 °C for 5 min, then 90 °C for 5 min). The lysate was clarified by filtration through a 0.45 μm Acrodisc syringe filter to remove residual sponge fragments. For protein quantification, 150 μL of filtrate was mixed with 150 μL of Coomassie Brilliant Blue G-250 reagent (50 mg mL⁻¹; Sigma) in a 96-well plate, gently shaken for 10 s, and incubated for 10 min at room temperature. Absorbance at 595 nm (OD₅₉₅) was measured using a multi-mode plate reader (TECAN Spark 10M). Protein concentration was obtained from a BSA standard curve prepared with the same diluent and processing steps across a concentration gradient.

Nafion membrane preparation

To protonate the Nafion 117 membrane for the MFC,¹⁹ we first washed it with deionised (DI) water 2–3 times. Then, the membrane was sequentially soaked in DI water at 80 °C for 1 h, 3% H₂O₂ at 80 °C for 1 h, and 1 M H₂SO₄ at 80 °C for 1 h. After that, the membrane was fully protonated, and it was finally washed with water 2–3 times to remove the chemicals from it. The Nafion membrane is kept in the DI water.



Microbial fuel cell experiment

Before the electrochemical experiments, the glass chambers are autoclaved and soaked in 70% ethanol for sterilisation. The electrodes were soaked in 70% ethanol for 20 minutes to sterilise. After that, they were rinsed in DI water for 10 minutes before soaking in the culture medium of *S. oneidensis* MR-1 for another 20 minutes. Then we put the bioanode into the anodic chamber.

The H-shaped two-chamber MFC is constructed by connecting two 25 mL chambers with a proton exchange membrane (PEM) Nafion 117 separator. Before the test, the anodic solution is purged with pure N_2 for 30 min to remove the dissolved oxygen. All MFC experiments are operated at room temperature. At MFC steady state, the polarisation curves are obtained by varying the external resistor. The output current is calculated from Ohm's Law: $I = V/R$ (R is the value of the external resistor). $P = IV = V^2/R^{-1}$ calculates the output power. Coulombic efficiency was calculated as a relationship between experimental coulombic efficiency and theoretical coulombic efficiency in accordance with ref. 2. For the mediator MFC setup, the cathode solution is changed to potassium ferricyanide ($K_3[Fe(CN)_6]$, 50 mM) and potassium chloride (KCl, 50 mM).

Evaluation of bacterial viability by confocal microscopy

Before testing, the bioanodes are first stained with 5 mM propidium iodide (PI, in SBM with 10 mM sodium (L)-lactate) for 10 min and rinsed with SBM containing 10 mM sodium (L)-lactate for 10 min, and then stained with 10 mM 4',6-diamidino-2-phenylindole (DAPI, in SBM with 10 mM lactate) for 20 min and subjected to the same rinsing for 20 min. PI is used to stain only the dead cells, and DAPI is used to stain all cells, including the viable and dead cells.

Results and discussion

S. oneidensis MR-1 culturing on the graphene sponge electrode

Previously, we demonstrated¹⁸ that the reduction temperature of the graphene oxide sponge strongly influences the surface hydrophobicity/hydrophilicity (Fig. 1 and S1). Mild thermal reduction at 375 °C provides an optimal balance of surface hydrophilicity and conductivity (10.61 S m^{-1}), as confirmed by X-ray photoelectron spectroscopy (XPS), X-ray diffraction (XRD), and contact angle measurements, which show a clear increase in the C/O ratio (5.51) and a corresponding contact angle of 78.9°. Compared with carbon fiber ($1 \text{ m}^2 \text{ g}^{-1}$), the graphene sponge offers a much higher surface area of $139.2 \text{ m}^2 \text{ g}^{-1}$. Half-cell electrochemical tests (Fig. S1) further reveal higher current output for the graphene sponge reduced at 375 °C due to enhanced bacterial growth (Table S1). Therefore, in the following experiments we used the 375 °C-reduced graphene oxide sponge. To fabricate a graphene sponge bioanode, *S. oneidensis* MR-1 was cultivated on the electrode surface to enable efficient charge transfer from the bacteria to the circuit, which is the source of MFC current and power.

Although graphene sponge is often perceived to exhibit membrane stress that could physically damage bacteria and cause cell membrane disintegration, our results show that it does not significantly affect bacterial viability.^{20–22} Alive–dead staining assay reveals distinct green fluorescence, which originates from the PI dye in the living bacteria, indicating the presence of alive bacteria on the surface only (Fig. 2a (inset)). In our previous studies, we have determined that the hydrophobic/hydrophilic balance is a key parameter to be considered for the optimization of bacterial attachment to the anode surface and thus, improved extracellular electron transfer.

Scanning electron microscopy (SEM) images further expose greatly variable bacterial density (Fig. 2a and b). Bar-like bacteria ($\sim 0.5 \mu\text{m}$ by $\sim 2 \mu\text{m}$) are found on the graphene sponge electrodes (Fig. 2a and b), whereas a few microorganisms are formed on carbon fiber (Fig. S2). These SEM studies are broadly consistent with the confocal fluorescence results and show that the presence of the graphitic surface is favourable to condensed bacteria seeding. The prevailing hydrophilicity of graphene sponge provides better adsorption and bacterial growth and leads to the facilitated direct electron transfer from bacteria to the electrode. As depicted in Fig. 2c the charge transfer resistance for the graphene sponge bioanode is 96Ω . The half cell experiments (Fig. 2d) demonstrate the high and stable current generation for 5 days.

Cathode ORR catalytic activity of graphene sponge

The MFC construction, besides the anodic electron transfer reaction from *S. oneidensis* MR-1, also requires a cathodic counterreaction to provide electromotive force. The greatest

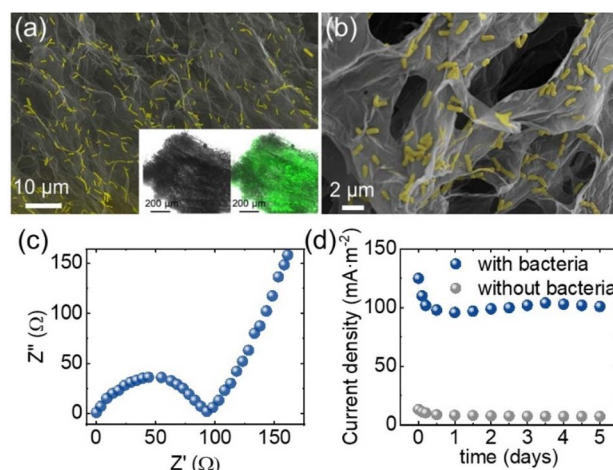


Fig. 2 Characterization of *S. oneidensis* MR-1 biofilms. (a and b) Scanning electron microscopy (SEM) images of graphene sponge covered by *S. oneidensis* MR-1. Confocal microscopy images of *S. oneidensis* MR-1 on graphene sponge with and without the DAPI filter (inset). (c) Electrochemical impedance spectroscopy: Nyquist curves of the graphene bioanodes, Z' and $-Z''$ are the real and imaginary parts of the impedance respectively. (d) 5-day chronoamperometry (CA) performance (under a bias voltage of 0.2 V vs. Ag/AgCl reference) of the graphene sponge without bacteria control (grey curve), the graphene bioanodes (blue curve). (c and d) Reprinted with permission from ref. 18.

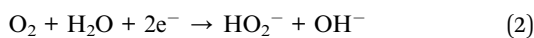


effectiveness of the MFC can be achieved if oxygen reduction is used as a counterreaction. Platinum-based catalysts are most widely used to provide high current efficiency.²³ However, using platinum-based catalysts in the MFC structure under realistic environmental conditions does not allow for the creation of biodegradable and easily recyclable MFCs as it is difficult to recycle the platinum from the MFC structure. Graphitic surface, due to its structure and functional groups, can also be used as a catalyst for the ORR.^{23–26} To provide an understanding of the role of the graphene sponge catalyst loading in the ORR electrochemical process, we investigated its electrocatalytic properties.

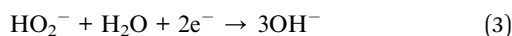
We carried out linear sweep voltammetry (LSV) measurements of the graphene sponge in an O₂-saturated 0.1 M KOH electrolyte solution. The results demonstrated a pronounced oxygen reduction. As shown in Fig. 3, the onset potentials of the ORR on the graphene sponge were comparable to those of the Pt electrode, although the Pt electrode exhibited a lower current density. For the graphene sponge electrode, the characteristic two-step pathway was observed, with onset potentials at approximately 0.7 and 1.2 V (*vs.* RHE), consistent with a successive two-electron transfer process.^{26–28}

In contrast, the carbon cloth electrode demonstrates the absence of two-electron transfer and low-current ORR. The Tafel slope for the rGO sponge is 98 mV dec⁻¹, which closely aligns with the measured value for the Pt electrode (80 mV dec⁻¹) and previously reported values for Pt/C electrodes (65–82 mV dec⁻¹).¹⁹

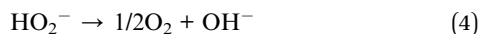
The ORR in alkaline solutions can proceed by two major pathways: a direct four-electron pathway and a two-electron 'peroxide' pathway according to eqn (1) and (2):



The peroxide (HO₂⁻) can then be reduced in accordance with the two-electron reaction:



or by the disproportionation process:



It is worth noting that the sum of the two sequential two-electron reductions (involving peroxide) (eqn (3) and (4)) leads to the respective four-electron reductions. The proposed graphene sponge with a higher electrocatalytic activity towards the ORR demonstrates an earlier onset potential and a higher current density. Compared with graphene sponge, the carbon cloth shows a dramatically increased current similar to the Pt electrode; this is mainly related to the higher resistance of the carbon cloth. The change in the shape of the voltammograms depicts the increase in the non-faradaic currents induced by the increase in the effective surface area of the electrically conductive graphene that is generated by the reduction of GO. As shown in Fig. 3b, the Tafel slope for the ORR of the graphene sponge electrode commenced at around -98 mV dec⁻¹, whereas the Tafel slope for the ORR of the carbon cloth electrode is -169 mV dec⁻¹. For the graphene sponge and Pt electrodes, a clear reduction pre-wave was observed at low overpotentials, followed by a second reduction wave starting at around 1.2 V, which is indicative of a prevalent two-electron reduction pathway. The absence of the peak in the LSV curve of carbon cloth at 1.2 V (Fig. 3a) shows that graphene sponge demonstrates a more efficient oxygen reduction, which could be due to the presence of nitrogen-related electrocatalytic active sites for oxygen reduction. The XPS data in Fig. 1 depict the presence of these groups in graphene sponge.

We have shown that graphene sponge represents enhanced catalytic activity towards the oxygen reduction reaction compared to the carbon cloth and the bare Pt electrode. However, its ORR activity is inferior to that of Pt catalysts, such as carbon black loaded with Pt particles. Kinetic studies disclosed that even if both the graphene sponge and bare Pt catalysts operate in combined 4e and 2e ORR processes, the graphene sponge follows a more predominant 2e pathway. This ORR pathway in graphene sponge has been related to the unreduced quinone functional groups, which favour the 2e ORR process. Thus, it is possible to use the graphene sponge as the cathode for the ORR in an MFC design.

MFC tests and performance

Before constructing full MFCs, the output current density of the anode materials was already evaluated with a three-electrode system in an electrochemical half-cell.¹⁸ Markedly, the maximum current density output from the graphene sponge electrode can reach up to 135.35 mA m⁻², which is considerably higher than that from either graphite felt (120 mA m⁻²)²⁹ or GO (17 mA m⁻²)³⁰ electrodes.

For the MFC power output evaluation, we have constructed the full-cell MFC device in a double-chamber container (Fig. 1b and 4). The output voltage from the MFC increases continuously with incubation time and reaches a nearly constant value in around 2 days (Fig. 4e), indicating the successful fabrication of a MFC.³¹

When the MFC voltage output is stable, different load resistors are connected to the anode and the cathode to obtain



Fig. 3 ORR catalytic properties of graphene-based thin-wall scaffolds. (a) Linear sweep voltammograms (LSVs) of the ORR in 0.1 M KOH for the carbon cloth, rGO sponge, and bare Pt electrodes. (b) Calculated Tafel slope values from LSV for the carbon cloth, rGO sponge, and bare Pt electrodes.





Fig. 4 (a) Polarization curve for the MFC with the carbon cloth cathode and bioanode. (b) Polarization curve for the MFC with the graphene sponge cathode and bioanode. (c) Polarization curve for the $K_3Fe(CN)_6$ -mediated MFC with the carbon cloth cathode and bioanode. (d) Polarization curve for the $K_3Fe(CN)_6$ -mediated MFC with the graphene sponge cathode and bioanode. (e) Voltage recorded for the MFC with a carbon cloth cathode (grey curve) and with graphene sponge cathode (blue curve). (f) MFC current density vs. time curves for long-term stability and repeated cycling tests of carbon cloth. (g) MFC current density vs. time curves for long-term stability and repeated cycling tests of the graphene sponge cathode and bioanode.

current vs. voltage (I - V) curves and power polarisation curves (Fig. 4a and b). The I - V curves demonstrate an identical open-circuit voltage of around 0.6 V for graphene sponge, which is consistent with the maximum voltage output from similar MFCs. For the carbon cloth-based MFC, the potential is as low as 0.3 V, which causes low ORR catalytic activity of carbon cloth. Notably, the graphene sponge electrode shows a maximum current output of $112.7 \mu A cm^{-2}$ (Fig. 4b), which is much higher than that of carbon cloth ($1.3 \mu A cm^{-2}$) (Fig. 4a). The power density for the graphene sponge electrode reaches $36.2 \mu W cm^{-2}$, which is also a much higher value than that for the carbon cloth electrode ($0.27 \mu W cm^{-2}$) (Fig. 4a and b).

In addition, we studied the case involving the replacement of the direct ORR with the mediator-based ORR in a cathodic chamber. Potassium hexacyanoferrate is the commonly used mediator in MFCs due to its chemical stability over time. Fig. 4c and d shows the polarisation curves for graphene sponge and carbon cloth electrodes. When using a mediator in MFC with graphene sponge and carbon cloth, the cell potential reaches 0.47 and 0.55 V, respectively. The power output also increases to $180 \mu W cm^{-2}$ for graphene sponge and to $130 \mu W cm^{-2}$ for carbon cloth. However, introducing an inorganic mediator prevents the creation of biodegradable and easily recyclable MFCs.

The obtained MFC output surpasses that of the MFC with the Pt/C cathode (Fig. S3), which yields $1.25 \mu A cm^{-2}$ current density and $0.2 \mu W cm^{-2}$ power.

The coulombic efficiency (CE), output power, and current observed for the graphene sponge are also higher than those

reported previously with other electrode materials (Table S2). We observe that utilizing a graphene sponge material as both the cathode and anode enables the attainment of coulombic efficiency, power density, and current output comparable to Pt cathode MFCs.

We have also evaluated the output performance of the proposed graphene sponge electrode in the ORR without a mediator over a long-term operation (Fig. 4f and g). Current output from the MFC decreases strongly after around 90 h of stable operation, which can be attributed to the nutrient consumption in the anode chamber.

We performed a cyclic test by periodically feeding the anodic medium with nutrients when the current output decreased (Fig. 4f and g).

After adding lactate as the nutrient to the anodic chamber, the output current density rapidly returned to its original value, which verified that the current drop is due to nutrient utilisation. Similar behaviour is observed for MFC with carbon cloth (Fig. 4f). Based on the amount of lactate added and total charge output for each cycle (Fig. 4f and g), we can also derive the coulombic efficiency of the MFCs.^{1,32} The MFC with graphene sponge shows a coulombic efficiency of around 70% (Table S2), which specifies efficient use of the lactate for power production. The microorganism contents of the graphene sponge and carbon fiber are 1.12 and 0.06 μg respectively (Table S1). The smaller number of bacteria on the carbon fiber is due to the high hydrophobicity of the carbon fiber surface (120°), while for the graphene sponge the hydrophobicity is 80° . Despite this, the carbon fiber also demonstrates some power



output due to the indirect electron transfer from bacteria. The increased current density from the graphene sponge could be attributed to a larger number of bacteria in the anode biofilm and to more-efficient charge transport and less charge loss due to the improved charge-transfer process and efficient catalytic ORR reaction on the graphene sponge electrode.

Conclusions

In summary, we demonstrated 3D graphene sponge as a novel and high-performance universal functional material, both as the anode and cathode of MFCs with stability up to 400 h. The MFCs armed with the graphene sponge reach a current density of $753 \mu\text{A cm}^{-2}$ and generate a maximum power density of $184 \mu\text{W cm}^{-2}$ in sodium lactate medium, which is comparable with that obtained from Pt-based cathodes and nanostructured anodes under the same conditions. Graphene sponge enables recyclable MFCs without any pollutants or difficult-to-recover materials or elements. The present study brings MFC technology closer to practical application.

Author contributions

K. N. conducted experiments and data analysis of this study and wrote the draft of the manuscript. L. X. and J. W. contributed to the bioelectrochemical experiments and related analysis. S. R. M. contributed to the bioelectrochemical experiments, quantification of bacteria, fluorescence microscopy, and analysis of bioelectrochemical performance. R. J. V. contributed to the discussion of conceiving this study. G. C. B., K. S. N., and D. V. A. conceived this work, contributed to data analysis, and revised the manuscript.

Conflicts of interest

The authors declare no competing interests.

Data availability

The data supporting the current study are available from the corresponding author upon reasonable request.

Supplementary information is available: detailed data on the optimization of the GO sponge reduction process as well as a comparison between carbon cloth and graphene sponge with respect to bacterial compatibility. See DOI: <https://doi.org/10.1039/d5su00629e>.

Acknowledgements

This work was supported by the Ministry of Education (Singapore) through the Research Centre of Excellence program (grant EDUN C-33-18-279-V12, I-FIM).

References

1 B. Cao, Z. Zhao, L. Peng, H.-Y. Shiu, M. Ding, F. Song, X. Guan, C. K. Lee, J. Huang, D. Zhu, X. Fu, G. C. L. Wong,

- C. Liu, K. Neelson, P. S. Weiss, X. Duan and Y. Huang, *Science*, 2021, **373**, 1336–1340.
- 2 S. Zhao, Y. Li, H. Yin, Z. Liu, E. Luan, F. Zhao, Z. Tang and S. Liu, *Sci. Adv.*, 2015, **1**, e1500372.
- 3 K. Kordek-Khalil, E. Altiok, A. Salvian, A. Siekierka, R. Torres-Mendieta, C. Avignone-Rossa, A. Pietrelli, S. Gadkari, I. A. Ieropoulos and F. Yalcinkaya, *Sustain. Energy Fuels*, 2023, **7**, 5608–5624.
- 4 Y. Yang, L.-N. Liu, H. Tian, A. I. Cooper and R. S. Sprick, *Energy Environ. Sci.*, 2023, **16**, 4305–4319.
- 5 J. Zhang, F. Li, D. Liu, Q. Liu and H. Song, *Chem. Soc. Rev.*, 2024, **53**, 1375–1446.
- 6 Y.-J. Jiang, S. Hui, S. Tian, Z. Chen, Y. Chai, L.-P. Jiang, J.-R. Zhang and J.-J. Zhu, *Nanoscale Adv.*, 2023, **5**, 124–132.
- 7 A. B. Jorge and R. Hazael, *Macromol. Chem. Phys.*, 2016, **217**, 1431–1438.
- 8 S. R. Juliastuti, R. Darmawan, A. Ayuningtyas and N. Ellyza, *IOP Conf. Ser. Mater. Sci. Eng.*, 2018, **334**, 012067.
- 9 D. V. Andreeva, M. Trushin, A. Nikitina, M. C. F. Costa, P. V. Cherepanov, M. Holwill, S. Chen, K. Yang, S. W. Chee, U. Mirsaidov, A. H. Castro Neto and K. S. Novoselov, *Nat. Nanotechnol.*, 2021, **16**, 174–180.
- 10 F. V. Lavrentev, I. S. Rumyantsev, A. S. Ivanov, V. V. Shilovskikh, O. Y. Orlova, K. G. Nikolaev, D. V. Andreeva and E. V. Skorb, *ACS Appl. Mater. Interfaces*, 2022, **14**, 7321–7328.
- 11 D. V. Andreeva and K. S. Novoselov, *Natl. Sci. Rev.*, 2022, **9**, nwab095.
- 12 M. H. Islam, S. Afroj, M. A. Uddin, D. V. Andreeva, K. S. Novoselov and N. Karim, *Adv. Funct. Mater.*, 2022, **32**, 2205723.
- 13 K. Yang, Z. Hu, X. Li, K. Nikolaev, G. K. Hong, N. Mamchik, I. Erofeev, U. M. Mirsaidov, A. H. Castro Neto, D. J. Blackwood, D. G. Shchukin, M. Trushin, K. S. Novoselov and D. V. Andreeva, *Proc. Natl. Acad. Sci. U. S. A.*, 2023, **120**, e2307618120.
- 14 F. H. Abrha, T. H. Wondimu, M. H. Kahsay, F. Fufa Bakare, D. M. Andoshe and J. Y. Kim, *Nanoscale*, 2023, **15**, 18184–18197.
- 15 Q. Adfar, S. Hussain and S. S. Maktedar, *New J. Chem.*, 2025, **49**, 2511–2650.
- 16 N. Garino, A. Sacco, M. Castellino, J. A. Muñoz-Tabares, A. Chiodoni, V. Agostino, V. Margaria, M. Gerosa, G. Massaglia and M. Quaglio, *ACS Appl. Mater. Interfaces*, 2016, **8**, 4633–4643.
- 17 R. Yadav, A. Subhash, N. Chemmenchery and B. Kandasubramanian, *Ind. Eng. Chem. Res.*, 2018, **57**, 9333–9350.
- 18 X. Leng, R. J. Vazquez, S. R. McCuskey, G. Quek, Y. Su, K. G. Nikolaev, M. C. F. Costa, S. Chen, M. Chen, K. Yang, J. Zhao, M. Lin, Z. Chen, G. C. Bazan, K. S. Novoselov and D. V. Andreeva, *Carbon*, 2023, **205**, 33–39.
- 19 L. Geniès, R. Faure and R. Durand, *Electrochim. Acta*, 1998, **44**, 1317–1327.
- 20 Y. Zang, B. Cao, H. Zhao, B. Xie, Y. Ge, H. Liu and Y. Yi, *Environ. Sci.: Processes Impacts*, 2023, **25**, 1863–1877.



- 21 C. Yang, H. Aslan, P. Zhang, S. Zhu, Y. Xiao, L. Chen, N. Khan, T. Boesen, Y. Wang, Y. Liu, L. Wang, Y. Sun, Y. Feng, F. Besenbacher, F. Zhao and M. Yu, *Nat. Commun.*, 2020, **11**, 1379.
- 22 S. Ikeda, Y. Takamatsu, M. Tsuchiya, K. Suga, Y. Tanaka, A. Kouzuma and K. Watanabe, *Essays Biochem.*, 2021, **65**, 355–364.
- 23 X.-X. Lin, A.-J. Wang, K.-M. Fang, J. Yuan and J.-J. Feng, *ACS Sustain. Chem. Eng.*, 2017, **5**, 8675–8683.
- 24 S. Pal, S. Bawari, T. Veetil Vineesh, N. Shyaga and T. N. Narayanan, *ACS Appl. Energy Mater.*, 2019, **2**, 3624–3632.
- 25 Z. Li, Q. Gao, H. Zhang, W. Tian, Y. Tan, W. Qian and Z. Liu, *Sci. Rep.*, 2017, **7**, 43352.
- 26 P. Yaengthip, A. Siyasukh, L. Payattikul, T. Kiatsiriroat and K. Punyawudho, *J. Electroanal. Chem.*, 2022, **915**, 116366.
- 27 S. K. Bikkarolla, P. Cumpson, P. Joseph and P. Papakonstantinou, *Faraday Discuss.*, 2014, **173**, 415–428.
- 28 Á. Ganyecz and M. Kállay, *J. Phys. Chem. C*, 2021, **125**, 8551–8561.
- 29 E. Kipf, J. Koch, B. Geiger, J. Erben, K. Richter, J. Gescher, R. Zengerle and S. Kerzenmacher, *Bioresour. Technol.*, 2013, **146**, 386–392.
- 30 A. A. Yaqoob, M. N. M. Ibrahim, A. S. Yaakop, K. Umar and A. Ahmad, *Chem. Eng. J.*, 2021, **417**, 128052.
- 31 H. N. Dai, T.-A. Duong Nguyen, L.-P. My Le, M. V. Tran, T.-H. Lan and C.-T. Wang, *Int. J. Hydrogen Energy*, 2021, **46**, 16612–16621.
- 32 T. N.-D. Cao, S.-S. Chen, H.-M. Chang, T. X. Bui and I. C. Chien, *Environ. Sci.: Water Res. Technol.*, 2020, **6**, 2776–2788.

